Received: 8 September 2018 | Revised: 10 December 2018 | Accepted: 11 December 2018

DOI: 10.4218/etrij.2018-0505

SPECIAL ISSUE

WILEY ETRI Journal

Holographic tomography: hardware and software solutions for 3D quantitative biomedical imaging (Invited paper)

Arkadiusz Kuś | Wojciech Krauze | Piotr L. Makowski | Małgorzata Kujawińska

Warsaw University of Technology, Institute of Micromechanics and Photonics, Warsaw, Poland.

Correspondence
Arkadiusz Kuś, Warsaw University of Technology, Institute of Micromechanics and Photonics, Warsaw, Poland.
Email: a.kus@mchtr.pw.edu.pl

Funding information
This work was supported by the *TEAM TECH programme of Foundation for Polish Science*, Poland, co-financed with the support of the European Union, Regional Development Fund (*TEAM TECH/2016-1/4, BiOpTo*).

In this paper, we demonstrate the current concepts in holographic tomography (HT) realized within limited angular range with illumination scanning. The presented solutions are based on the work performed at Warsaw University of Technology in Poland and put in context with the state of the art in HT. Along with the theoretical framework for HT, the optimum reconstruction process and data visualization are described in detail. The paper is concluded with the description of hardware configuration and the visualization of tomographic reconstruction, which is calculated using a provided processing path.

KEYWORDS
holographic tomography, optical diffraction tomography, tomographic phase microscopy, cell refractive index, 3D imaging

1 | INTRODUCTION

The noninvasive imaging of microbiological samples plays a crucial role in the research on the pathophysiology of human diseases [1,2]. In particular, the possibility of the quantitative three-dimensional (3D) representation of living samples holds tremendous potential for advancing the field as it would provide unprecedented ease of insight into subtle intracellular mechanisms. Presently, various techniques of quantitative phase microscopy (QPM) are used to achieve this goal [3]. Amplitude and phase profiles demodulated from digital holographic measurements are commonly used for the automated assessment of the statistical properties of cell cultures [4,5]. However, owing to the integrated character of the data delivered by holography, QPM has limited capabilities for providing full 3D structural information. Depth-resolved microscopy or the tomographic versions of QPM are applied to overcome this limitation. The first group of methods includes different realizations of confocal fluorescence microscopy [6–8]. They provide high specificity owing to the application of a wide range of fluorescent biomarkers and the nanometer-range resolution uniformly distributed across a sample volume. However, measurements are not label free and they are time-consuming because of the point-by-point scanning scheme and sample preparation procedures. In contrast, tomographic phase microscopy (TPM) [9,10] represents a wide range of label-free methods that aim to reconstruct the volumetric distribution of refractive index (RI) or, equivalently, dry mass density inside a sample [11,12,2], thus providing a nonspecific but directly quantitative and dynamic counterpart to 3D fluorescent images [13]. This has been achieved with various degrees of success through inverse scattering solutions, such as classical optical diffraction tomography (ODT) [14,15] and its more sophisticated variants supported by compressive sensing techniques [16,17], complex deconvolution [18], and nonlinear forward models [19]. TPM also includes axial-scanning-based methods that involve broadband illumination [20,21] and/or spatially incoherent illumination [22–24]. Within TPM, coherent linear ODT represents the oldest and best-established technique, which has recently created

and demonstrated numerous possibilities for the 3D imaging of live cells [13,25]. This is already reflected by the commercial devices that utilize this framework and are targeted specifically for microbiological research, namely, the products of NanoLive, Ltd [26] and TomoCube, Inc. [27]. In this work, we summarize the current status of classical ODT from a metrological perspective in microbiological studies. More specifically, the laser-driven limited-angle variant of ODT (LAODT) in the scanning illumination configuration is considered. This method is relatively easy to implement and appropriate for the characterization of adhesive cells and cell cultures directly on a Petri dish. We discuss the inherent limitations of this approach from the perspectives of hardware and software [28] with emphasis on the quality of depth reconstruction. Then, we review a few practical strategies to circumvent the limitations with minimal system complexity and cost, including the solutions developed by our group [29,30,31,32]. Section 2 briefly states the theoretical basis of LAODT with emphasis on the practical effects of involved approximations in the context of cytology. In Section 3, we present the well-known variants of the LAODT system configuration and discuss the aspects of holographic data acquisition. Section 4 describes selected numerical processing paths optimized for microbiological measurements. The corresponding reconstruction results are compared in Section 5. Section 6 summarizes the capabilities and limitations of the state-of-the-art solutions in LAODT. In addition, we outline future prospects for further improvements of the technique that should lead to marketable products that provide 3D RI reconstructions of living cells with rapid acquisition rates and practical levels of resolution uniformity.

2 | ODT FRAMEWORK

In this section, the theory of LAODT [33] is presented with focus on the source of "missing cone" artifacts, anisotropic resolution, and Fourier spectrum mapping errors. The description is partially based on [34]. To retrieve information about the RI of an investigated sample, the inverse problem of reconstructing an object function from a set of object projections recorded by a camera must be solved. The first step is always to retrieve the scattered field, $u_s(\mathbf{r})$, which is exclusively associated with the investigated sample and related with the total field, $u(\mathbf{r})$, captured by the camera according to (1).

$$u(\mathbf{r}) = u_0(\mathbf{r}) + u_s(\mathbf{r}), \tag{1}$$

where $u_0(\mathbf{r})$ is the incident field, which propagates unperturbed in free space. To retrieve $u_s(\mathbf{r})$, we employ the first-order Rytov approximation, in which the total field, $u(\mathbf{r})$, is represented in the following form:

$$u(\mathbf{r}) = \exp(\Psi(\mathbf{r})), \tag{2}$$

where Ψ is referred to as the complex phase function. By analogy to (1), the complex phase of the total field can be represented as the sum of the complex phases associated with the incident field ($\Psi_0(\mathbf{r})$) and scattered field ($\Psi_s(\mathbf{r})$).

$$\Psi(\mathbf{r}) = \Psi_0(\mathbf{r}) + \Psi_s(\mathbf{r}). \tag{3}$$

The Rytov approximation allows for the calculation of $\Psi_s(\mathbf{r})$ as

$$\Psi_s(\mathbf{r}) = \frac{1}{u_0(\mathbf{r})} \int G(|\mathbf{r} - \mathbf{r}'|) f(\mathbf{r}') u_0(\mathbf{r}') d^3\mathbf{r}', \tag{4}$$

where $G(\mathbf{r})$ is the Green's function and $f(\mathbf{r})$ is the scattering potential, which is defined as

$$f(\mathbf{r}) = k_m^2 \left[\left(\frac{n(\mathbf{r})}{n_m} \right)^2 - 1 \right], \tag{5}$$

where n_m is the RI of the immersion medium, k_m is the wavenumber of the immersion medium, and $n(\mathbf{r})$ is the absolute RI of the sample given by $n(\mathbf{r}) = n_m + n_\sigma(\mathbf{r})$. $n_\sigma(\mathbf{r})$ is the local deviation of the RI of the propagation medium from n_m, and it is associated with the presence of the investigated sample in the measurement volume. λ_0 is wavelength of the utilized light in vacuum.

The Rytov approximation can be successfully performed when the gradient of the complex phase is small. As the complex phase gradient does not depend on the thickness of an analyzed sample, the applicability condition for the Rytov approximation is independent of object size. Additionally, it should be noted that the $u_0(\mathbf{r})$ field must be measured to calculate the complex phase, $\Psi_s(\mathbf{r})$. This is realized by capturing the projections of the measurement volume with no object present, which are referred to as reference projections.

The Rytov approximation enables us to calculate the complex phase, $\Psi_s(\mathbf{r})$, from each object projection captured by a detector. The Fourier diffraction theorem (FDT) can be used to calculate the 3D RI distribution of an analyzed sample from these fields [35]. When a specimen is illuminated by a plane wave, the FDT relates the two-dimensional (2D) Fourier transform of the complex phase, $\Psi_s(\mathbf{r})$, with a spherical surface (referred to as the Ewald sphere) in the 3D Fourier transform of the scattering potential of the analyzed sample. If the sample is conjugated with a detector plane through a microscope objective, the FDT is described as (6) (the relation for 2D tomography has been shown for the sake of simplicity).

$$\hat{\Psi}_s(\alpha) = \frac{j}{2\sqrt{k_m^2 - \alpha^2}} \hat{f}(\alpha, \sqrt{k_m^2 - \alpha^2} - k_m), \quad \text{for } |\alpha| < k_m \tag{6}$$

where $\hat{\Psi}_s$ and $\hat{f}$ are the Fourier transforms of Ψ_s and f, respectively, and α is the lateral spatial frequency coordinate.

The FDT for LAODT is schematically presented in Figure 1. When the illumination direction is altered and consecutive projections are captured, the Fourier spectrum is filled with the Fourier transforms of the scattered fields that are cast onto shifted arcs. The filled spectrum is presented in Figure 1C. When all projections are processed, the spectrum is inverse Fourier transformed, and the scattering potential of the sample is reconstructed. The described procedure is a basic tomographic reconstruction algorithm named direct inversion. A 2D tomography case is shown in Figure 1. However, in the paper, all tomographic reconstruction procedures utilize the 3D FDT, where each complex phase is a 2D field and its Fourier transform is cast onto a 3D spherical cap [36,37].

However, despite indisputable advantages, the operating principle of LAODT is a source of its biggest drawback. Owing to the fact that the detector is stationary during the measurement process and the illumination is rotating, there is a limited angular range of illumination directions within which the projections can be acquired. This is caused by the limited numerical aperture (NA) of the microscope objective in the imaging system. As a consequence, when all projections are captured by the LAODT setup and the spectrum of the reconstruction is filled with their Fourier transforms according to the FDT, a relatively large area of the spectrum still remains empty. As presented in Figure 1C, no information about spatial frequencies is provided in the cone around the γ axis. Thus, in LAODT, it is not possible to fill the spectrum completely. This inherent property of LAODT results in highly distorted tomographic reconstructions of analyzed samples along the optical axis of an optical system when simple reconstruction procedures, such as direct inversion, are used. This is the first source of errors in LAODT. This problem may be solved by utilizing a hybrid approach, that is, combining rotation and illumination scanning [38]. The LAODT illumination scanning projections of the sample may be acquired for several angles of orientation of the object. Then, all LAODT data sets may be combined in the Fourier domain to obtain isotropic reconstruction resolution. Alternatively, one can use object rotation instead of the scanning of illumination to provide quasi-uniform resolution. One of the interesting solutions would be to rotate cells by tumbling during their flow [39]. However, this does not prevent the mechanical perturbation of the measured biological object.

Another problem associated with LAODT is the anisotropic resolution of reconstruction along the optical axis. The resolution is the maximum in the region of reconstruction that is within the depth of field (DOF) of a utilized microscope objective and decreases as the distance from this region increases. This is caused by the utilization of the Rytov approximation in the tomographic reconstruction process. However, there is considerable confusion in research papers regarding this subject. In particular, numerous sources claim that the Rytov approximation has spatially invariant accuracy. Reference [37] states that "This condition basically asserts that the Rytov approximation is independent of the specimen size and only limited by the phase gradient (...)." Furthermore, [40] states that "(...) the size of the scatterer is not a factor in determining the accuracy of the Rytov approximation." These statements are not precise and may lead to incorrect conclusions. While it is true that the validity condition for the Rytov approximation is associated only with the phase gradient (unlike the Born approximation), it is not equivalent to the fact that a 3D reconstruction calculated with the Rytov approximation will have a uniform resolution in the entire measurement volume. This is only the condition for the type of object that can be reconstructed with this approximation. The Rytov

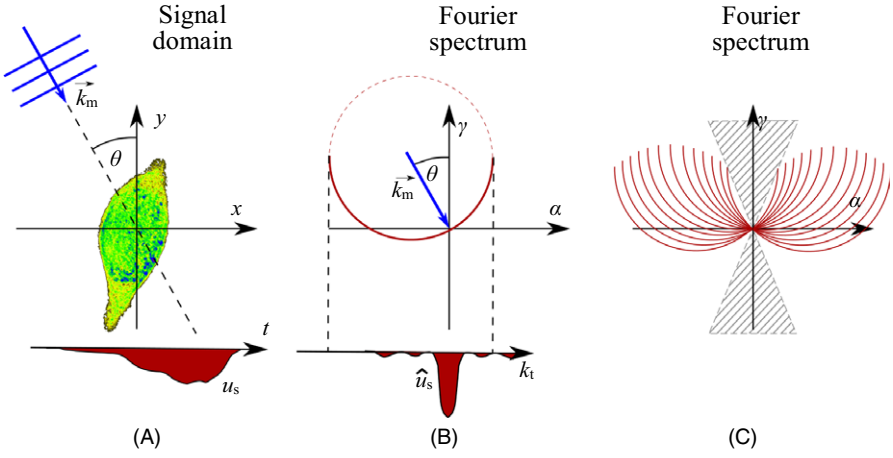

FIGURE 1 Visualization of the FDT for LAODT. (A) Projection acquisition configuration; (B) corresponding arc in the Fourier spectrum of the object's scattering potential; (C) example of a spectrum filled with data from multiple projections (the gray sector represents an empty region in the spectrum) [Colour figure can be viewed at wileyonlinelibrary.com]

approximation is carried out by removing the component with the gradient of the complex phase from the Helmholtz equation. This operation can be successfully performed when this gradient is small (only then the approximation holds). Consequently, the gradient of the complex phase is small when the gradient of the RI distribution in the measurement volume is small. Note that if the gradient of the object's RI distribution is small, the gradient of the Rytov field emitted by a selected object plane will be small regardless of the thickness of the object. In this sense, the Rytov approximation does not depend on object size. This can be compared with the Born approximation, which depends on the total energy of the scattered field. However, in the Rytov approximation, the simplified Helmholtz equation is used to propagate the complex field and to calculate the tomographic reconstruction. As this is not a rigorous propagation algorithm, it introduces errors that increase with the propagation distance from the plane that is conjugated with the camera. As a result, in LAODT, the resolution of the reconstruction decreases as the distance from the focal plane in the object space increases.

As seen from the above discussion, there are several fundamental phenomena in the limited angle tomographic reconstruction of optical transparent microstructures that influence the final accuracy of 3D RI distribution. Only a deep understanding of these phenomena, a fully conscious design of holographic tomography (HT) microscopes and projection capturing scenarios, and creating a full processing path from sinograms to 3D RI reconstruction will allow for high quality results and ensure their quantitative character. For this reason, in the subsequent sections, we present the HT systems and software solutions that ensure quantitative LAODT reconstructions to the best of our knowledge.

3 | HARDWARE

To provide measurement data for HT, it is essential to deliver a set of complex amplitudes acquired within a range of viewing angles, which are later processed with a tomographic solver. This imposes the first two requirements for hardware, that is, system configuration and a scanning module. While lensless tomographic systems have already been developed [41], the most common system type is a digital holographic microscope with a detector conjugate to a sample plane in a Mach-Zehnder (MZ) [36,42,43,18] or common-path interferometer configuration [44,45]. The MZ configuration is particularly suitable for phase object analysis. However, MZ-based systems are inherently prone to external disturbances. This is in contrast to common-path systems, which provide more robustness. The drawback of the latter is that if a large shear between object and image beams is used to create a hologram [44], there is a chance of two objects overlapping and rendering measurement impossible, even if measurement objects are placed sparsely in the region of interest. Other common-path systems use a replica of an object beam, which must be filtered with an additional spatial filter to provide a reference beam [46]. This solution is difficult to implement for tomography. Despite the decreased stability, MZ systems are the most suitable for phase object analysis and have already been used in commercial solutions such as NanoLive [26] and TomoCube[27] products. For this reason, this paper is limited to the MZ-based tomographs.

In the second step, the systems are modified to provide a variable illumination angle in the object beam.

To provide a set of projections acquired at different viewing angles without moving the measured object, an HT system requires a beam tilting component and an optical system with a high NA for illumination and imaging. This implies either a condenser lens for illumination and a microscope objective for imaging (MO and CL in Figure 2A) or two microscope objectives (Figure 2B). In general, optical systems with an NA of at least 0.8 are used. However, the NA typically exceeds 1.2 [28] in oil or water immersion objectives. This provides a maximum illumination angle ranging from 45° up to even 60° or 70° [43,47]. As a basic beam tilting solution, a motorized mirror can be placed in a plane conjugate to the measured object and camera[48,36]. A more advanced system would use galvanometer mirrors [43,49], as indicated by GM in Figures 2A and B, to reduce measurement time. Alternatively, different concepts such as mechanical scanning using a rotating prism can be employed. Such concepts have already been successfully introduced [18,50].

A simple idea of changing the illumination angle in the object beam leads to consequences in complex amplitude retrieval for the projections in MZ-based systems. The fringe period in each hologram changes with the angle between the object and reference beams. To successfully retrieve the complex amplitude in any illumination direction allowed by the system, either a temporal phase shifting approach could be used [36,43] or projections would have to be acquired for a quasi-constant fringe period. Such a condition is automatically achieved when the object beam is scanned around a cone (or a circle in the front focal plane of the illuminating objective). However, this limits the amount of data that can be acquired at intermediate azimuth angles and affects the quality of reconstruction [31]. For this reason, a second motorized mirror is additionally placed in the system in a few cases [45,42], for example, TM in Figure 2A, or other scanning strategies are applied, such as grid [31] or spiral scanning [42,44]. A new common-scan type of system has been built to prevent the addition of more moving components [31], as shown in

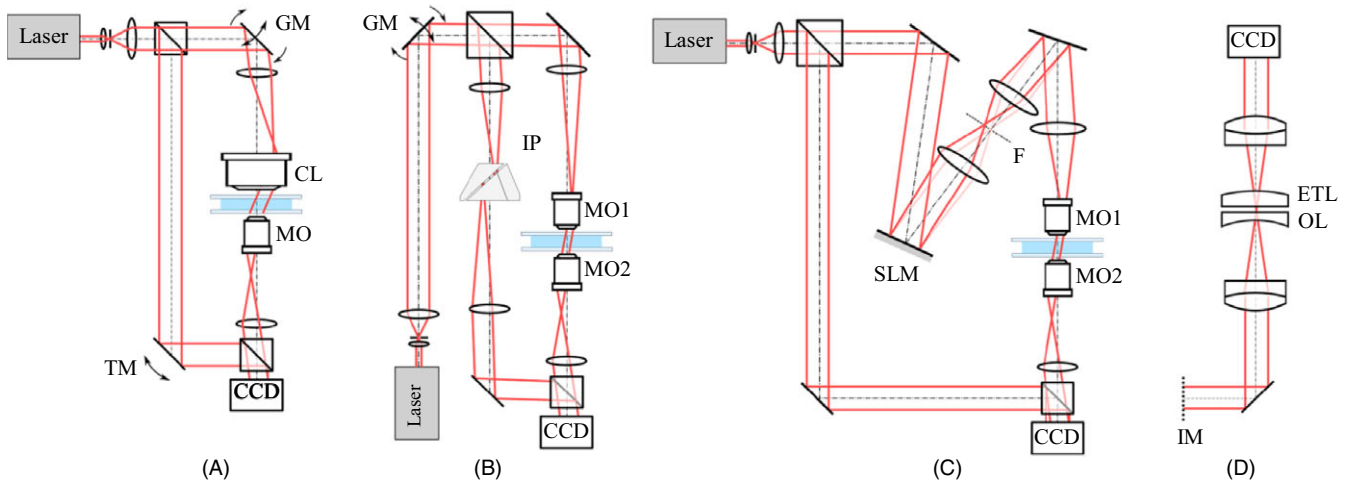

FIGURE 2 Typical holographic tomography measurement system setups based on Mach-Zehnder configuration. (A) Scanning with a galvanometer mirror (GM); (B) common-scan configuration; (C) scanning using a spatial light modulator; (D) extended depth of field module [Colour figure can be viewed at wileyonlinelibrary.com]

Figure 2B. In this system, the beam splitter for the MZ configuration is placed after the beam has passed through a dual-axis galvanometer mirror. The magnification between the galvanometer mirror and detector is the same for the object and reference beams. This is ensured by two lenses and an inverting prism. This minimizes the cost of the otherwise more complex optical system. As a result, the relative angle between the two beams is quasi-constant. Moreover, the fringe period can be matched to the optical system and detector and maintained constant for the entire measurement regardless of the object's illumination angle.

Still, the scanning provided by mechanically moved components may be questionable and may introduce additional errors [28] resulting from lack of mechanical stability and the repeatability of the galvanometer mirror [51]. As a result, a number of movement-free systems, such as those shown in Figure 2C, have been developed. In the aforementioned figure, beam tilting (scanning) is performed using a spatial light modulator, which may be a liquid crystal on silicon modulator [52] or a digital micromirror device [53,54] in this case. Such an approach leads to improved scanning repeatability and stability [51] and a more accurate tomographic reconstruction [28]. Moreover, the quality of the illumination system resulting from scanning component flatness may degrade the reconstruction result in a few cases. Therefore, placing an active beam steering device in the system provides an opportunity to correct the illuminating wavefront [28].

To provide the best quality reconstruction with HT, it is vital to maximize the illumination angle and thus the NA of the optical system (imaging and illumination). This leads to a highly limited DOF, which degrades the result. To further improve reconstruction quality, it is possible to extend the DOF in reconstruction either numerically [49] or using a hardware approach [30]. The computational enhancement based on numerical defocusing provides outstanding improvement [49]. However, the calculations are time-consuming and the equivalent hardware solution may be obtained at additional measurement time instead [55,30]. The hardware approach requires an additional module, as shown by the extension presented in Figure 2D, added to an HT system instead of a camera. IM in the figure represents an intermediate image plane, and ETL is a tunable lens combined with OL, which is an offset lens. Such an afocal system allows for the movement of the plane conjugate to the camera. One can combine the partial reconstruction into an enhanced result by obtaining a set of projections at different focus settings.

4 | SOFTWARE

In this section, the numerical procedures and methods for the 3D tomographic reconstruction of biological specimens are presented.

As described in Section 2, the most basic tomographic reconstruction algorithm that considers diffraction is direct inversion. However, highly distorted results are obtained when this method is applied to the data acquired using the LAODT system. Thus, numerous iterative algorithms with constraints applied in each iteration are reported in literature. The most frequently used approach is the Gerchberg-Papoulis (GP) method, which is described in section 4.1, where the solution to the data mapping problem is also proposed. In section 4.2, a more advanced method dedicated to the analysis of biological samples with nonpiecewise-constant RI distribution is presented. In section 4.3, a numerical procedure for the minimization of the

reconstruction artifacts that are due to the limited DOF of the optical setup (as described in Section 2) is provided.

4.1 | Gerchberg-Papoulis algorithm

In its basic form, the modified GP algorithm for ODT consists of the following four steps [56,47]:

(i) $F'_j = (1 - \beta\Omega)F_{j-1} + \beta\Omega F_0$
(ii) $f_j = \mathrm{IFFT}\{F'_j\}$
(iii) $f'_j = g^{-1}\left(P_\beta P_+ \Re\{g(f_j)\}\right)$
(iv) $F_j = \mathrm{FFT}\{f'_j\}$.

Step (i) describes the replenishment of the 3D spatial frequency domain, F, of the object scattering potential, f (see (5)) with projection data stored in F_0. Only the known voxels of F_0 are replaced, which are represented here by the binary substitution mask, Ω. The F_0 array is built once before the iterations start by mapping the 2D projection spectra on their corresponding Ewald spheres using the nearest neighbor method. In this process, the values of overlapping voxels are averaged, which prevents the overrepresentation of low frequencies in F_0. Step (iii) applies the nonnegativity constraint to the j'th reconstruction. Function $g(\cdot)$ returns the complex RI minus the immersion level for a given f (5). $\Re$ takes the real value of its argument and operator P_+ replaces negative values with zeros. β is an optional relaxation parameter that is gradually decreased during iterations (eg, by $\beta_j = 0.99\beta_{j-1}$). This parameter acts as a weight for data replenishment in (i) and simultaneously suppresses object space padding in (iii) performed by operator P_β, which multiplies padded regions by $(1 - \beta)$. Object padding is the signal domain extension that follows from Fourier domain oversampling defined as $\alpha = N_\mathrm{F}/N_\mathrm{p}$, where N_F and N_p denote the pixel sizes of the 3D spatial frequency array and 2D projection array, respectively.

The optimal operational conditions of the GP algorithm are rarely discussed in literature. It is worth noting that this method is generally accurate only with spatially bound objects (such as individual cells or isolated groups) that occupy a fraction of the horizontal field of view (FoV) of size $N_\mathrm{p} \times N_\mathrm{p}$ and surrounded with a clear immersion medium. There are two reasons for this. First, if the object profile fits the entire projection frame (detector area), it implies that the diffraction tails of the object wavefield have been cut out. Incomplete projections typically cause the algorithm to converge to a distorted solution. Second, the relative size of the object within the 3D FoV corresponds to the sampling density of its spatial frequency content. If the signal is smaller with respect to the window, its spectrum varies more slowly. Effectively, the nearest neighbor strategy during the initial assembly of F_0 introduces less distortion. In practice, interpolation-related artifacts are frequently still visible even with the FoV two times wider than the object. For this reason, additional spectrum oversampling (α) is frequently employed. In classical ODT with object rotation, this is best achieved via projection padding. However, in LAODT, considerable memory and computation effort can be saved by leaving the projections intact and instead applying a finer sampling of F only in its vertical axis, perpendicular to the fixed detector plane. The reconstruction quality is almost the same in both cases, with significant improvement starting from $\alpha = 2.0$. More efficient strategies for the minimization of interpolation errors within the GP scheme have also been reported [57,58]; however, they are outside the scope of LAODT. Another potentially attractive direction for improvement in LAODT is the use of the joint sparsification of the wavelet coefficient and gradient domains. This has already proved to be useful in providing diagnostic quality reconstructions in magnetic resonance imaging from strongly sparse data that do not conform well to the piecewise constancy condition enforced by total variation (TV) regularization [58].

With complete and clean projections and sufficient sampling density in F, the GP algorithm tends to converge reliably and independent of data resolution and content. Therefore, for a given illumination pattern, a fixed number of iterations between 100 and 200 should be sufficient. An automatic stop condition can be also employed, for instance, by detecting saturation in the slope of the relative change between consecutive reconstructions.

It is possible to supplement the GP algorithm with various regularization schemes simply by applying additional constraints in step (iii). In [56], the authors use a nested gradient descent loop to minimize the TV norm just before the next forward Fourier transform. The work [16] reviews a few other propositions that incorporate TV regularization into the ODT framework in a more robust manner. However, the results are visibly affected by the stairway artifacts characteristic for TV minimization, which tends to the obscure the finer details of typical microbiological samples. In the following section, we outline a different proposition of utilizing TV in LAODT [29,30], which can be based on any iterative algorithm with spatial support capability, including the basic GP scheme described above.

4.2 | Total variation iterative constraint algorithm

The TV iterative constraint (TVIC) method is a tomographic reconstruction strategy that can be combined with the arbitrary iterative algorithm. It provides increased reconstruction quality with highly minimized LAODT artifacts [29]. Therefore, the method solves the main LAODT problem, that is, the "missing cone" problem outlined in

Section 2. When the TVIC method is combined with the GP algorithm (TVIC-GP), it does not assume any specific RI distribution of analyzed samples (like piecewise constancy), and thus, it is used for the analysis of biological specimens, where it provides superior quality compared to the GP algorithm alone.

The TVIC method is a two-stage iterative strategy. In the first stage, a support constraint is automatically generated. Then, it is passed to the second stage, that is, the GP algorithm described in section 4.1 (however, any algorithm can be selected).

The TV minimization algorithm is applied along with the algebraic reconstruction method to generate the support constraint [59,60,61,62]. The problem can be stated as follows:

$$\begin{array}{ll} \underset{\mathbf{f}}{\text{minimize}} & \|\mathbf{f}\|_{\text{TV}} \\ \text{subject to} & A\mathbf{f} = \mathbf{b} \quad \mathbf{f}_j \geq 0 \end{array}, \tag{7}$$

where $\mathbf{f}$ is the reconstruction function, f, represented in the vector form, $\mathbf{f}_j$ are the elements of the vector with $j = 1, 2, \ldots N$, N is the total number of voxels in the reconstruction, A is the forward projection operator, $\mathbf{b}$ is the sinogram with measurement data represented in the vector form, where the elements of the vector are $\mathbf{b}_j$ with $j = 1, 2, \ldots M$, and M is the total number of pixels in all acquired projections. The minimization in (7) is constrained with two conditions. The first, $A\mathbf{f} = \mathbf{b}$, forces the resulting reconstruction to be consistent with the sinogram. The second, $\mathbf{f}_j \geq 0$, is the nonnegativity condition that uses *a priori* knowledge that the phase values in the reconstruction cannot be negative.

Technically, the minimization in (7) can be carried out using various optimization algorithms. In this paper, the Chambolle-Pock method is used, in which operator A is defined like in computed tomography [63,64].

The result of applying TV minimization is a 3D reconstruction of the measured biological microsample, which contains erroneous RI values because TV minimization assumes piecewise constancy of the RI distribution. However, the boundaries of the sample are correctly retrieved, free from the distortion characteristic of LAODT. This reconstruction defines the spatial limits of the specimen. Thus, the RI distribution is binarized, and a 3D mask of an object, that is, the support constraint, is created. Then, this mask is passed to the GP algorithm described in section 4.1, where it is applied in each iteration of the tomographic reconstruction along with the nonnegativity constraint. As piecewise constancy is not assumed in the GP algorithm, the method is applied to biological microsamples with arbitrary RI distributions. The utilization of the precisely generated support constraint in the GP algorithm results in reconstructions in which the two most visible LAODT artifacts are corrected, namely, decrease in RI values close to object boundaries and elongation of specimen boundaries in the direction of the optical axis. The superiority of this combined approach over the standard GP method is shown in Section 5.

It is important to note that the TVIC method, like any other support-constraint-based approach, is sensitive to the structures in the measurement volume that are not covered by the 3D mask. The presence of such structures (such as cellular debris, dust particles, or even other surrounding cells) results in decreased reconstruction quality. However, in recent years, a sinogram preprocessing method has been proposed to remove these unwanted inclusions [65].

It should be noted that other reconstruction strategies have also been proposed in recent years. An iterative approach for reconstructing data from tomography that combines the object rotation and axial scanning of a sample is presented in [66]. In [67], the authors propose a nonlinear and computationally efficient reconstruction algorithm that considers multiple scattering. In [68], the vectorial treatment of captured data is used, thus allowing for the utilization of polarization effects.

4.3 | Extended depth-of-field tomography

In Section 2, the reconstruction error associated with the limited DOF of the LAODT setup was described. In Section 3, a modification of the optical setup was proposed to capture multiple sets of object projections for different positions of focal planes. In this section, a numerical procedure for processing data is presented. This procedure allows for the calculation of 3D tomographic reconstructions with quasi-isotropic resolution in structures with relatively large depth.

The complete description of the numerical solution, referred to as extended DOF tomography (EDOFT), is presented in [30]. The inputs to the algorithm are object sinograms, where each sinogram is captured for a different position of a focal plane in the object space. The motivation behind this approach is that when a tomographic reconstruction is calculated with the Rytov approximation, only the fragment that surrounds the plane that corresponds to the focal plane in the object space of the optical setup is reconstructed with isotropic resolution.

During calculations, each sinogram is independently reconstructed using the TVIC-GP approach described in section 4.2. As a result, a set of tomographic reconstructions is obtained. In each reconstruction, each region has different isotropic resolution (the depth of this region depends on the type of investigated specimen and the NA of the microscope objective). Thus, it is clear that the input sinograms should be captured in such a manner that the fragments with isotropic resolution from all reconstructions should cover the entire volume of the investigated sample. The fragments with

isotropic resolution are cut out from each reconstruction. Finally, all fragments are stitched into a new tomographic reconstruction, where isotropic resolution is maintained throughout the volume of the analyzed specimen.

It should be noted that the presented approach is not the only solution to anisotropic resolution in tomographic reconstructions that is associated with the limited DOF of an optical setup. Another approach is a purely numerical solution in which each projection is rigorously propagated to multiple planes that cover the range of the entire sample [49]. In the next step, complex phases, $\Psi_s(\mathbf{r})$ (see Section 2), are calculated from the propagated fields and the final reconstruction is obtained. This method requires capturing only a single set of projections, which is a significant advantage. However, it involves extensive and time-consuming data processing.

The increase in reconstruction quality due to the utilization of EDOFT is shown in Section 5.

5 | RESULTS

5.1 | Investigated object and experimental system

To visualize the effect of the numerical procedures described in this paper on tomographic reconstruction quality, a biological specimen was investigated with a LAODT system and reconstructed using three different approaches. The selected specimen was a mouse fibroblast cell from the 3T3 cell line [69]. The cells were cultured on a glass bottom dish with a diameter of 35 mm (Ibidi, Germany) in DMEM supplemented with 10% fetal calf serum, 4 mM glutamine, penicillin, and streptomycin in a humidified incubator at 37°C and 7.5% CO2.

The tomographic projections were captured by utilizing the system presented in Figure 2B with an extended DOF module (Figure 2D) placed between the image plane and camera. A He-Ne laser at $\lambda = 632.8$ nm was used as a coherent light source. At each focal plane position set by the tunable lens, 360 holograms were acquired with the conical illumination scenario at 1° intervals and a zenith angle of 52°. The NAs of the illumination and imaging systems were 1.3 each (100x microscopes objectives). Then, each hologram was processed using the Fourier transform phase retrieval algorithm [70] to obtain the complex amplitude for each viewing direction. The complex amplitudes were filtered with a [3 × 3] median filter to reduce noise in the reconstruction.

5.2 | Tools for 3D visualization

One of the common problems of all tomographic techniques is the 3D visualization of reconstructions. The optimal software tool must be user-friendly, compatible with common tomographic file formats (such as Matlab or RAW files), and should provide visualizations that allow for the clear presentation of the inner structures of the investigated sample. The possibility of preparing movies is an additional advantage. Two such tools are the Drishti volume exploration and presentation tool [71] and Tomviz [72]. Both tools are free and relatively easy to use. In Drishti, to visualize the data saved in a Matlab file, the data must be first exported into a RAW file and then converted from the RAW format into the format read by the software, which is realized by a separate tool distributed along with the main application. In the next step, the converted data are imported into Drishti, where visualization parameters can be specified. The graphical user interface (GUI) requires practice; however, it provides a significant number of visualization options (including slicing and movie generation). In Tomviz, the data can be imported into the main application directly, without the additional conversion step. The GUI does not require experience from the user, and it provides a similar number of visualization options as Drishti.

5.3 | Measurement results of a biological cell

The tomographic data of the fibroblast cell, which were captured in the system described in section 5.1, are reconstructed using three approaches. The first is the GP algorithm described in section 4.1 using the z-direction upsampling of $\alpha = 2.0$. The result obtained after 100 iterations of the GP method is presented in Figures 3A and B, where the y-x and y-z cross sections of the 3D reconstruction are shown. It can be noted that the boundary of the cell is blurred in the z direction, and only one high-RI structure is visible.

In Figures 3C and D, the reconstruction calculated with the GP method supported with the TVIC strategy is presented. The comparison of this result with the previous result leads to the following three conclusions: (i) the object boundaries become sharp, (ii) the average RI increases, and (iii) the second high-RI structure becomes visible. However, the pseudopod, which is visible on the right side of the cell, looks less natural.

The last result, shown in Figures 3E and F, is calculated using the TVIC-GP procedure but with the EDOFT approach. Four focal planes that are evenly distributed and cover the entire object volume are used. For each focal plane, a 3D reconstruction is calculated with the TVIC-GP algorithm and the region surrounding the focal plane is cut out. Finally, all cut-out fragments are stitched. It is clear that this approach combines the advantages of the TVIC-GP method without introducing new artifacts (the pseudopod regains its correct shape). A 3D Tomviz visualization of this reconstruction is shown in Figure 3G.

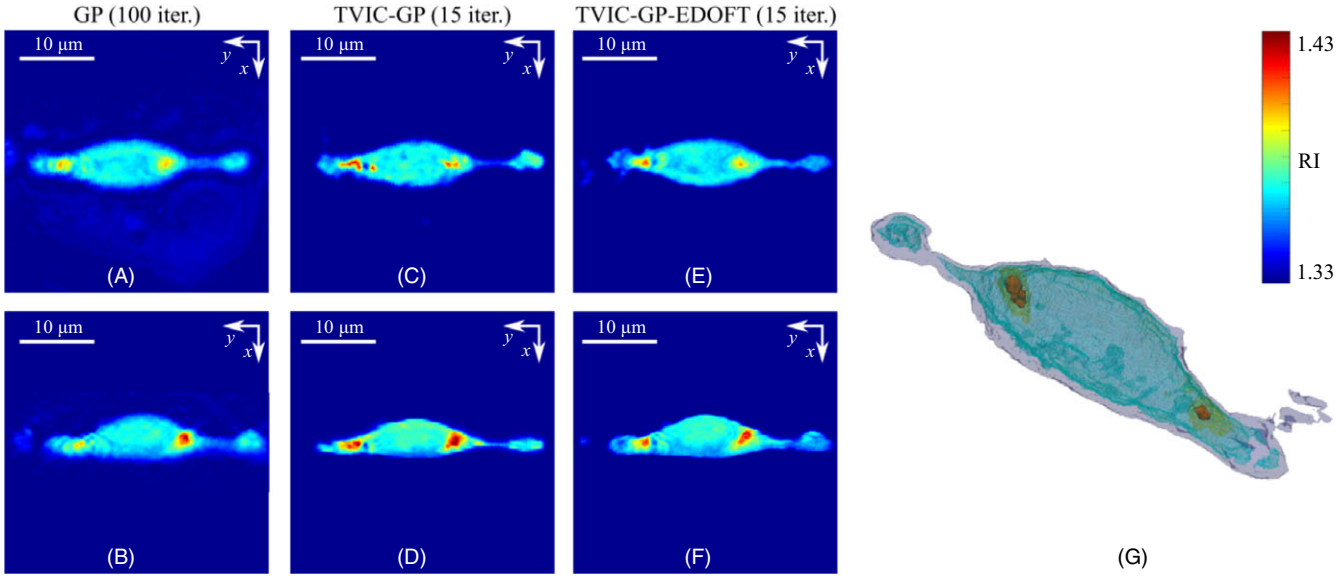

FIGURE 3 Comparison of 3D tomographic reconstructions of a 3T3 cell calculated with (A-B) GP, (C-D) TVIC-GP, and (E-F) TVIC-GP-EDOFT with four focal plane approaches. (G) 3D visualization of the TVIC-GP-EDOFT reconstruction [Colour figure can be viewed at wile yonlinelibrary.com]

6 | CONCLUSIONS

In recent years, rapid developments in the field of quantitative phase imaging have produced a large number of innovative optical imaging techniques, all of which compete for future adoption in biomedical sciences. In the context of volumetric imaging, the ODT approach is currently the most developed method, and it has already been represented in the market for 3D microscopes. The products available currently are based on classical (linear and coherent) ODT in the limited angle configuration. The *NanoLive* device uses the complex deconvolution of projection fields to enhance resolution in a single-step direct inversion reconstruction. In contrast, *TomoCube* utilizes GP iterations for reducing the image deformations and resolution inhomogeneity caused by missing projection angles. Different hardware solutions are utilized to realize illumination beam scanning, such as a spinning mirror (*NanoLive*) or a digital micromirror device (*TomoCube*). Even though both commercial products provide a certain degree of depth resolution, reconstruction quality decreases quite rapidly as the distance from the main focal plane increases. Thus, the removal of limited angle artifacts remains an open practical problem. Various regularization algorithms have been proposed (mainly based on TV minimization) to resolve this problem, but their applicability to arbitrary microbiological structures remains questionable owing to the side effects involved.

The processing path outlined in this work presents a complete instrumental/numerical solution dedicated specifically to the imaging of biological cells. The solution overcomes the abovementioned metrological limitations. In particular, the overall geometry and RI levels in the underestimated regions (not fully recovered through the nonnegativity condition alone) are corrected, bringing the result closer to its intended quantitative character. This includes counteracting the "depth of focus" problem that stems from the Rytov weak scattering approximation. We mention two effective methods of approaching this issue, that is, a hardware approach and a software approach. The practical conditions for the effective application of the GP algorithm are also described in detail. In addition, we refer to a possible improvement in GP-based LAODT in terms of the Fourier domain interpolation accuracy and a flexible wavelet-based regularization scheme, which has already been applied in 3D medical imaging.

In conclusion, coherent LAODT has already proven to be a practical method for label-free microbiological imaging. Even though a number of new promising methods have been introduced in recent years, particularly partially coherent ODT, the classical LAODT scheme is currently the most reliable. A number of technically attractive improvements to current commercial products can be proposed based on literature, which would bring the method significantly closer to the highly desired status of a full-3D quantitative technique. For this reason, one can expect that future 3D microscopes based on the classical LAODT framework will continue to take lead in terms of overall 3D imaging accuracy.

ACKNOWLEDGEMENTS

The research leading to the described results was carried out within the program TEAM TECH/2016-1/4 of

Foundation for Polish Science, co-financed by the European Union under the European Regional Development Fund. The authors acknowledge the support from the statutory funds and the grants of the Dean of Mechatronics Faculty, Warsaw University of Technology.

REFERENCES

1. K. R. Lee et al., *Quantitative phase imaging techniques for the study of cell pathophysiology: From principles to applications*, Sensors (Basel, Switzerland) **13** (2013), 4170–4191.
2. Z. Wang et al., *Tissue refractive index as marker of disease*, J. Biomed. Opt. **16** (2011), no. 11, 116017.
3. G. Popescu, *Quantitative Phase Imaging of Cells and Tissues*, McGraw Hill Professional, March 2011.
4. B. Kemper et al., *Investigation of living pancreas tumor cells by digital holographic microscopy*y, J. Biomed. Opt. **11** (2006), no. 3, 34005.
5. P. Bon et al., *Quadriwave lateral shearing interferometry for quantitative phase microscopy of living cells*, Opt. Express **17** (2009), no. 15, 13080.
6. N. Streibl, *Three-dimensional imaging by a microscope*, JOSA A**2** (1985), no. 2, 121–127.
7. M. Oheim et al., *Principles of two-photon excitation fluorescence microscopy and other nonlinear imaging approaches*, Adv. Drug Deliv. Rev. **58** (2006), no. 7, 788–808.
8. B. M. Michalska et al., *Insight into the fission mechanism by quantitative characterization of Drp1 protein distribution in the living cell*, Scienti. Rep. **8** (2018), no. 8122, 1–15.
9. D. Jin et al., *Tomographic phase microscopy : Principles and applications in bioimaging*, JOSA B **34** (2017), no. 5, B64–B77.
10. G. Popescu and Y. Park, *Quantitative phase imaging in biomedicine*, Nat. Photon. **12** (2018), 578–589.
11. R. Barer, *Determination of Dry Mass, Thickness, Solid and Water Concentration in Living Cells*, Nature **172** (1953), no. 4389, 1097–1098.
12. G. Popescu et al., *Optical imaging of cell mass and growth dynamics*, Am. J. Physiol. Cell Physiol. **295** (2008), no. 2, 345–348.
13. K. Kim et al., *Optical diffraction tomography techniques for the study of cell pathophysiology*, J. Biomed. Photon. Eng. **2** (2016), no. 2, 020201.
14. O. Haeberlé et al., *Tomographic diffractive microscopy: Basics, techniques and perspectives*, J. Modern Opt. **57** (2010), no. 9, 686–699.
15. C. J. R. Sheppard and S. S. Kou, *3d imaging with holographic tomography*, AIP Conf. Proc. **1236** (2010), no. 1, 65–69.
16. J. W. Lim et al., *Comparative study of iterative reconstruction algorithms for missing cone problems in optical diffraction tomography*, Opt. Express **23** (2015), no. 13, 16933.
17. Y. Sung and R. R. Dasari, *Deterministic regularization of three-dimensional optical diffraction tomography*, JOSA A **28** (2011), no. 8, 1554–1561.
18. Y. Cotte et al., *Marker-free phase nanoscopy*, Nat. Photon. **7** (2013), 113–117.
19. H.-Y. Liu et al., *SEAGLE: Sparsity-Driven Image Reconstruction Under Multiple Scattering*, IEEE Trans. Comput. Imag. **4** (2018), no. 1, 73–86.
20. Z. Wang et al., *Spatial light interference tomography (SLIT)*, Opt. Express **19** (2011), no. 21, 19907.
21. P. Hosseini et al., *Scanning color optical tomography (scot)*, Opt. Express **23** (2015), no. 15, 19752–19762.
22. Y. Bao and T. K. Gaylord, *Quantitative phase imaging method based on an analytical nonparaxial partially coherent phase optical transfer function*, J. Opt. Soc. Am. A **33** (2016), no. 11, 2125.
23. M. Chen, L. Tian, and L. Waller, *3D differential phase contrast microscopy*, Biomed. Opt. Express **7** (2016), no. 10, 3940–3950.
24. J. M. Soto, J. A. Rodrigo, and T. Alieva, *Optical diffraction tomography with fully and partially coherent illumination in high numerical aperture label-free microscopy [Invited]*, Appl. Opt. **57** (2018), no. 1, A205.
25. B. Vinoth et al., *Integrated dual-tomography for refractive index analysis of free-floating single living cell with isotropic superresolution* , Scienti. Rep. **8** (2018), no. 1, 5943.
26. Nanolive Cell Explorer hardware description, http://nanolive.ch/hardware, 2018, Accessed: 2018-09-01.
27. Tomocube hardware description, http://www.tomocube.com/product/technology/, 2018, Accessed: 2018-09-01.
28. A. Kuś, *Illumination-related errors in limited-angle optical diffraction tomography*, Appl. Opt. **56**(2017), no. **33**, 9247–9256.
29. W. Krauze et al., *Generalized total variation iterative constraint strategy in limited angle optical diffraction tomography*, Opt. Express **24** (2016), no. **5**, 4924–4936.
30. W. Krauze et al., *Reconstruction method for extended depth-of-field optical diffraction tomography*, Methods **136** (2018), no. 1 March 2018, 40–49.
31. A. Kuś, P. L. Makowski, and M. Kujawińska, *Advances in design and testing of limited angle optical diffraction tomography system for biological applications*, Proc. SPIE **9718** (2016), 1–9.
32. J. Kostencka et al., *Accurate approach to capillary-supported optical diffraction tomography*, Opt. Express **23** (2015), no. 6, 7908–7923.
33. E. Wolf, *Three-dimensional structure determination of semi-transparent objects from holographic data*, Opt. Commun. **1** (1969), no. 4, 153–156.
34. W. Krauze, Method for the numerical analysis of phase biological microsamples in limited-angle optical tomography, Ph.D. thesis, Warsaw University of Technology, 2018.
35. A. C. Kak and M. Slaney, *Principles of computerized tomographic imaging*, SIAM, 2001.
36. V. Lauer, *New approach to optical diffraction tomography yielding a vector equation of diffraction tomography and a novel tomographic microscope*, J. Microsc. **205** (2002), no. 2, 165–176.
37. Y. Sung et al., *Optical diffraction tomography for high resolution live cell imaging*, Opt. Express **17** (2009), no. 1, 266–277.
38. B. Simon et al., *Tomographic diffractive microscopy with isotropic resolution*, Optica **4** (2017), no. 4, 460–463.
39. F. Merola et al., *Tomographic flow cytometry by digital holography*, Light Sci. Appl. **6** (2017), 1–7.
40. T. M. Habashy, R. W. Groom, and B. R. Spies, *Beyond the born and rytov approximations: A nonlinear approach to electromagnetic scattering*, J. Geophys. Res. **98** (1993), no. B2, 1759–1775.
41. S. O. Isikman et al., *Lens-free optical tomographic microscope with a large imaging volume on a chip*, Proc. Natl. Acad. Sci. USA **108** (2011), no. 18, 7296–301.
42. Y. Sung et al., *Stain-free quantification of chromosomes in live cells using regularized tomographic phase microscopy*, PloS ONE **7** (2012), no. 11, e49502.

43. W. Choi et al., *Tomographic phase microscopy*, Nat. Methods **4** (2007), no. 9, 717–719.
44. K. Kim et al., *Diffraction optical tomography using a quantitative phase imaging unit*, Opt. Lett. **39** (2014), no. 24, 6935–6938.
45. Y. Kim et al., *Profiling individual human red blood cells using common-path diffraction optical tomography*, Scienti. Rep. **4** (2014), 6659.
46. G. Popescu et al., *Diffraction phase microscopy for quantifying cell structure and dynamics*, Opt. Lett. **31** (2006), no. 6, 775–777.
47. K. Kim et al., *High-resolution three-dimensional imaging of red blood cells parasitized by Plasmodium falciparum and in situ hemozoin crystals using optical diffraction tomography*, J. Biomed. Opt. **19** (2014), no. 1, 011005.
48. W. Krauze, A. Kuś, and M. Kujawińska, *Limited-angle hybrid optical diffraction tomography system with total-variation-minimization-based reconstruction*, Opt. Eng. **54** (2015), 054104.
49. J. Kostencka et al., *Holographic tomography with scanning of illumination: Space-domain reconstruction for spatially invariant accuracy*, Biomed. Opt. Express **7** (2016), no. 10, 4086–4100.
50. S. Kawata et al., *Laser computed-tomography microscope*, Appl. Opt. **29** (1990), no. 26, 3805–3809.
51. S. Shin et al., *Optical diffraction tomography using a digital micromirror device for stable measurements of 4-D refractive index tomography of cells*, Proc. SPIE Int. Soc. Opt. Eng. **9718** (2016), no. 971814, 1–8.
52. A. Kuś, W. Krauze, and M. Kujawińska, *Active limited-angle tomographic phase microscope*, J. Biomed. Opt. **20** (2015), no. 11, 111216.
53. S. Shin et al., *Active illumination using a digital micromirror device for quantitative phase imaging*, Opt. Lett. **40** (2015), no. 22, 1–5.
54. K. R. Lee et al., *Time-multiplexed structured illumination using a DMD for optical diffraction tomography*, Opt. Lett. **42** (2017), no. 5, 999–1002.
55. A. Kuś, W. Krauze, and M. Kujawińska, *Focus-tunable lens in limited-angle holographic tomography*, Proc. SPIE **10070** (2017), 1–9.
56. S. J. LaRoque, E. Y. Sidky, and X. Pan, *Accurate image reconstruction from few-view and limited-angle data in diffraction tomography*, JOSA A **25** (2008), no. 7, 1772–1782.
57. A. Pryor et al., *GENFIRE: A generalized Fourier iterative reconstruction algorithm for high-resolution 3d imaging*, Scienti. Rep. **7** (2017), no. 1, 1–12.
58. P. L. Makowski, *Redundant Haar wavelet regularization in sparse-view optical diffraction tomography of microbiological structures*, Speckle 2018: VII International Conference on Speckle Metrology, vol. 10834, International Society for Optics and Photonics, Sept. 2018, p. 108341U.
59. A. Kuś et al., *Limited-angle hybrid diffraction tomography for biological samples*, Proc. SPIE **9132** (2014), 91320O.
60. E. Y. Sidky, C.-M. Kao, and X. Pan, *Accurate image reconstruction from few-views and limited-angle data in divergent-beam ct*, J. X-ray Sci. Technol. **14** (2006), no. 2, 119–139.
61. X. Jin et al., *Anisotropic total variation for limited-angle ct reconstruction*, Nuclear Science Symposium Conference Record (NSS/MIC), 2010 IEEE, IEEE, 2010, pp. 2232–2238.
62. A. Kuś, W. Krauze, and M. Kujawińska, *Limited-angle, holographic tomography with optically controlled projection generation*, Proc. SPIE **9330** (2015), 933007.
63. E. Y. Sidky, J. H. Jørgensen, and X. Pan, *Convex optimization problem prototyping for image reconstruction in computed tomography with the Chambolle–Pock algorithm*, Phys. Med. Biol. **57**(2012), no. 10, 3065.
64. A. Chambolle and T. Pock, *A first-order primal-dual algorithm for convex problems with applications to imaging*, J. Math. Imag. Vis. **40** (2011), no. 1, 120–145.
65. W. Krauze and M. Kujawińska, *Sinogram cleaning procedure for optical diffraction tomography*, Proc. SPIE 10834 (2018), no. 108341Q, 1–5.
66. Y. Bao and T. K. Gaylord, *Iterative optimization in tomographic deconvolution phase microscopy*, JOSA A **35** (2018), no. 4, 652–660.
67. E. Soubies, T.-A. Pham, and M. Unser, *Efficient inversion of multiple-scattering model for optical diffraction tomography*, Opt. Express **25** (2017), no. 18, 21786–21800.
68. C. Godavarthi et al., *Superresolution with full-polarized tomographic diffractive microscopy*, JOSA A **32** (2015), no. 2, 287–292.
69. H. Spielmann et al., *The international EU/COLIPA in vitro phototoxicity validation study: results of Phase II (blind trial). Part 1: The 3T3 NRU phototoxicity test*, Toxicol. In Vitro **12** (1998), no. 3, 305–327.
70. M. Takeda et al., *Fourier-transform method of fringe-pattern analysis for computer-based topography and interferometry*, J. Opt. Soc. Am. **72** (1982), no. 1, 156.
71. A. Limaye, *Drishti: A volume exploration and presentation tool*, Proc. SPIE **8506** (2018), 85060X.
72. B. D. A. Levin et al., *Tutorial on the visualization of volumetric data using tomviz*, Microsc. Today **26** (2018), no. 1, 12–17.

AUTHOR BIOGRAPHIES

Arkadiusz Kuś received his MSc Eng. degree in automation and robotics with specialization in photonics engineering from Warsaw University of Technology, Faculty of Mechatronics in 2012. In 2017 he received his PhD from the same faculty in 2017. He has been working for Warsaw University of Technology, Institute of Micromechanics and Photonics since 2015. First as research and teaching assistant and since 2018 as assistant professor. His current research interests include optical diffraction tomography, digital holographic microscopy, and optical design.

Wojciech Krauze received his MS degree in photonics engineering from the Warsaw University of Technology, Poland, in 2013. His PhD in the field of photonics engineering was defended at the same university in 2018. From 2011 to 2015 he worked at Warsaw

University of Technology in research projects, first as a student and later as a PhD student. Since 2018 he is hired as assistant professor at Warsaw University of Technology. His research interests include optical diffraction tomography applied to analysis of biological samples.

Piotr Leszek Makowski received his MSE degree in technical physics, specialty optoelectronics, from the Faculty of Physics at Warsaw University of Technology, Poland, in 2009. In 2013 he obtained the PhD-Eng degree in the field polarization and statistical optics at the same Faculty. During the studies he worked on contract in collaboration with the Faculty of Electronics and Information Technology, WUT. In 2013 he received a postdoctoral stipend at the Institute of Micromechanics and Photonics, Faculty of Mechatronics, WUT, where he presently holds a research fellow position. His current research interests are digital holography and optical diffraction tomography.

Małgorzata Kujawinska received her MS, PhD and DSc. in applied optics from the Faculty of Mechatronics, Warsaw University of Technology in 1976, 1982 and 1990, respectively SPIE Fellow. From 1976 she worked for Warsaw University of Technology, where she is now full Professor and the head of Photonics Engineering Division at Institute of Micromechanics and Photonics. She had also worked at National Physical Laboratory, UK (1986-1989). She had been the 2005 SPIE President and recipient of SPIE 2013 Chandra S. Vikram Award in Optical Metrology. Her main interest is full-field optical metrology and 3D imaging with special focus on holography.